A Fiber-Based Ratiometric Optical Cardiac Mapping Channel Using a Diffraction Grating and Split Detector

Ninita H. Brown,* Hana M. Dobrovolny,† Daniel J. Gauthier,† and Patrick D. Wolf*
*Department of Biomedical Engineering, and †Department of Physics, Duke University, Durham, North Carolina

ABSTRACT Optical fiber-based mapping systems are used to record the cardiac action potential (AP) throughout the myocardium. The optical AP contains a contraction-induced motion artifact (MA), which makes it difficult to accurately measure the action potential duration (APD). MA is removed by preventing contraction with electrical-mechanical uncoupling drugs, such as 2,3-butanedione monoxime (BDM). We designed a novel fiber-based ratiometric optical channel using a blue light emitting diode, a diffraction grating, and a split photodetector that can accurately measure the cardiac AP without the need for BDM. The channel was designed based on simulations using the optical design software ZEMAX. The channel has an electrical bandwidth of 150 Hz and an root mean-square dark noise of 742 μV. The channel successfully recorded the cardiac AP from the wall of five rabbit heart preparations without the use of BDM. After 20-point median filtering, the mean signal/noise ratio was 25.3 V/V. The APD measured from the base of a rabbit heart was 134 $\pm$ 8.4 ms, compared to 137.6 $\pm$ 3.3 ms from simultaneous microelectrode recordings. This difference was not statistically significant (p-value = 0.3). The quantity of MA removed was also measured using the motion ratio. The reduction in MA was significant (p-value = 0.0001). This fiber-based system is the first of its kind to enable optical APD measurements in the beating heart wall without the use of BDM.

INTRODUCTION

Optical recordings of the cardiac action potential (AP) have been traditionally limited to the epicardial surface. A more complete picture of the cardiac dynamics across the heart wall can be found using transmural fiber-based systems (1–5). These systems have been used to study the transmural action potential duration (APD), but the recordings contain a contraction-induced motion artifact (MA). MA is commonly removed by stopping contraction using drugs such as 2,3-butanedione monoxime (BDM) (6–9), calcium channel blockers (10), or cytochalasin-D (11). BDM has been shown to cause subtle changes in the APD and dynamic restitution, which are strongly dependent on the heart preparation, recording site, and species (12–20). Some limitations of BDM have been overcome by using cytochalasin-D (21,22), but it has also been shown to have effects on the tissue electrophysiology (17,23). An additional approach is mechanical restriction, which has been successful surface imaging in small heart (24). Lastly, MA has been reduced using a signal processing technique known as ratiometry (25,26). Ratiometry was first developed to image lipid vesicles and cultured HeLa cells (26). We have designed a novel ratiometric fiber-based channel using a royal blue light-emitting diode (LED), a diffraction grating, and a split photodetector.

A ratiometric signal is produced by taking the ratio of two simultaneously collected optical signals from wavelengths at opposite sides of the dye emission spectrum. This method relies on the fact that the entire emission spectrum shifts toward lower wavelengths during an AP (27), but the total emitted power stays constant. Knisley et al. applied ratiometry to optical recordings from the rabbit epicardium using a system that included a blue laser, a spectrograph, and a photodiode array (25). Caldwell et al. applied both ratiometry and subtraction to recordings from a fiber-based system that included a blue laser, a dichroic mirror, and multiple discrete photodiodes (2,3). Byars et al. also performed recording using a fiber-based system consisting of a mercury lamp, a dichroic mirror, and a photodiode array (1). The recordings from the fiber-based systems still contained MA that had to be further reduced using BDM.

The previously reported fiber-based ratiometric systems used a dichroic mirror to separate the dye emission light into two fixed wavelength bands (1–5). The two bands were then detected individually using separate channels. The fluorescent intensity from each of these bands was not equal, causing incomplete cancellation of the MA (28).

Our system uses a diffraction grating, which converts the wavelength-dependent shift during an AP into a spatial shift in the reflected intensity distribution. Changes in this intensity are detected by a split photodetector, where the split is centered near the peak of the emission spectrum. The increase in intensity at shorter wavelengths is measured on one photodiode cell, and the decrease in intensity at longer wavelengths is measured on the other photodiode cell. The specific wavelengths of detection are dependent on the location of the split photodetector with respect to the light reflected from the grating. By making small adjustments in the location of the split detector, the intensity variations due to motion can be minimized.

Submitted November 18, 2006, and accepted for publication February 22, 2007.

Address reprint requests to Ninita Brown, Department of Biomedical Engineering, 136 Hudson Hall, Duke University, Durham, NC 27708. E-mail: ninita.brown@duke.edu.

Editor: Raimond L. Winslow.

0006-3495/07/07/254/10 $2.00

doi: 10.1529/biophysj.106.101154

This work describes the simulations of the channel using the optical modeling software ZEMAX, the construction and alignment of the device with performance measurements, and the experimental testing in five rabbit studies. Our channel is compact and inexpensive compared to the previous systems. The total cost decreases by using a diffraction grating and a split photodetector, rather than a spectrograph and a detector array, respectively. This allows the channel to be expanded economically into a multichannel system.

METHODS

Optical channel

A schematic diagram of the optical channel is shown in Fig. 1.

The illumination pathway

A 125-μm core diameter fiber (CFO1493-09; OFS, Avon, CT) was butt-coupled to a royal blue LED (LXHL-LR3C; Lumileds Lighting, San Jose, CA). The LED was powered from a direct current power supply (GPS-3303; GW Instek, Chino, CA), which produced a constant current of 1 amp (*A*). The royal blue LED is a high-power, low-noise, inexpensive source that emitted light in a narrow wavelength band between 435 nm and 475 nm. A royal blue LED ($\lambda_{peak} = 455$ nm) was used because the absorption of the electrochromatic dye di-4-ANEPPS is greatest at blue wavelengths, close to the dye's absorption maximum (468 nm in bilayer) (29–31).

The fiber from the LED was terminated with a ferrule connector (FC), which was connected to the channel though a panel-mounted FC-FC connector (F1-FC6L; FIS, Oriskany, NY). This feature allowed for simple switching of the light source. Inside the panel, an additional FC-terminated fiber was connected to an aspheric lens collimation package (F230FC-A; Thorlabs, Newton, NJ), which collimated the light emerging from the fiber. Next, the light reflected off a dichroic mirror (515dcxr; Chroma Technology, Rockingham, VT), which transmitted light at wavelengths longer than 515 nm and reflected light at shorter wavelengths (*B*). The reflected illumination light was then focused by a second aspheric lens collimation package into another 125-μm core diameter tissue fiber (*C*). This optical fiber was terminated with an FC connector at the collimation package end but was left bare at the other end to insert into and illuminate the tissue. This light caused the dye, di-4-ANEPPS, to fluoresce from the cell membrane (*D*).

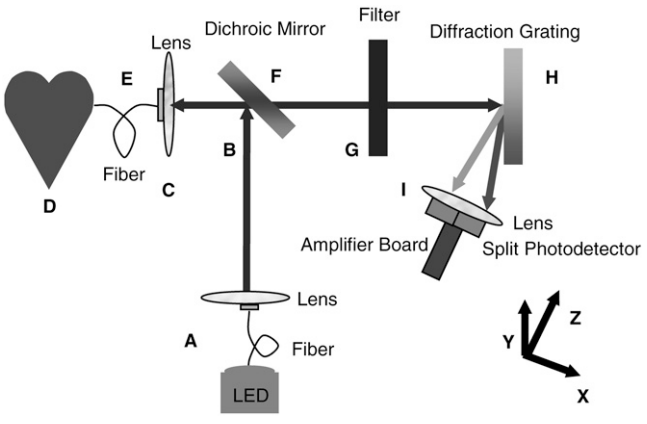

FIGURE 1 Schematic diagram of the fiber-based ratiometric optical channel. The labels *A–D* refer to the illumination pathway of the channel as described in the text. All lenses have a radius of 5 mm. The dichroic mirror and filter are 25 mm × 25 mm × 1 mm. The diffraction grating is 25 mm × 25 mm × 9.5 mm. The labels *E–I* refer to the detection pathway of the channel as described in the text. The *xyz* directions are also shown. The *y* direction is perpendicular to the *xz* image plane.

The detection pathway

The tissue fiber both transmitted the illumination light and received the emitted light. The bare end of the fiber was polished at a 45° angle to decrease back reflection from the excitation light (3,32) (*E*). The light collected by the fiber was transmitted through the dichroic mirror (*F*). The light was filtered to only transmit wavelengths above 530 nm using a long-pass filter (HQ530lp; Chroma Technology). This filter reduced reflected and scattered excitation light (*G*). The filtered light was reflected off an aluminum-coated diffraction grating (1200 grooves/mm, 43210; Edmund Industrial Optics, Barrington, NJ) (*H*). An additional aspheric lens (350330A; Thorlabs) focused the diffracted light onto a split photodetector (Spot2D; UDT Sensors, Hawthorne, CA) (*I*).

The highly sensitive split photodetector converted the emission light into two currents. The currents were converted into voltages using an ultralow bias current operational amplifier (OPA124U; Burr-Brown, Dallas, TX). Fig. 2 shows a schematic of the detection circuit.

The photodiodes operated in the photovoltaic mode to minimize the dark current and amplifier bias current (33). A 100-MΩ feedback resistor (R_f) was chosen to optimize the tradeoff between gain and noise to achieve the required bandwidth (1,34).

In stage 1, the photodiode current (*I*) was converted to voltage (*V*), as determined by

$$V = -R_f \times I. \quad (1)$$

In stage 2, the signal was multiplied by a gain *G*, as determined by

$$G = (1 + 100\,k\Omega/10\,k\Omega) = 11. \quad (2)$$

This circuit converted a current of 1 pA to a voltage of a 1.1 mV ($G = -1.1$ mV/pA).

Ray tracing simulations

Ray tracing simulations (ZEMAX Development, Bellevue, WA) were performed to optimize the geometry of the components in the detection pathway. The diffraction grating separated the emission light into different

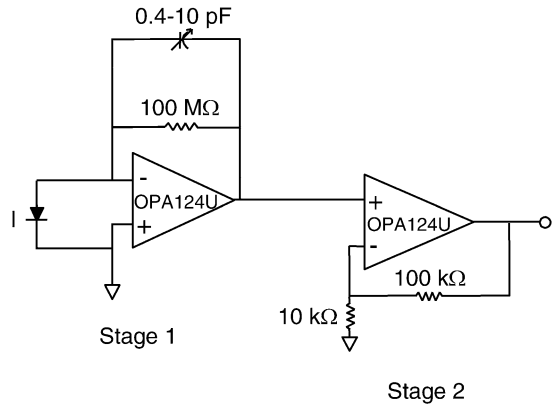

FIGURE 2 Amplification circuit. The photodiode current (I) is converted to a voltage by the 100-MΩ resistor in stage 1 using an operational amplifier (OPA124U, Burr-Brown Corp.). In stage 2, the signal is amplified using an additional operational amplifier (OPA124U, Burr-Brown Corp.).

wavelengths by reflecting the light at different angles. The angle of reflection θ was determined by

$$\theta = \sin^{-1}(n\lambda/d \pm \sin\theta_i), \quad (3)$$

where λ is the wavelength of the light, d is the grating constant, θ_i is the incident angle, and n is the diffraction order (35). The first order ($n = \pm 1$) was used because it is a principal maximum where the higher orders of diffraction do not overlap. The angle of incidence was set to zero degrees ($\theta_i = 0$) to maximize the angular dispersion.

The angular dispersion of a diffraction grating is determined by the inverse of the grating constant ($1/d$) or pitch. Commercially sold diffraction gratings at the dye emission wavelengths with a pitch of 600 grooves/mm or 1200 grooves/mm were simulated to select the optimal pitch. ZEMAX design software was used to simulate the emission pathway of the light by ray tracing a set of discrete wavelengths. We simulated 12 sample wavelengths spanning the emission spectrum of the dye. Each wavelength had an associated relative power, which was determined by the relative dye emission multiplied by the relative responsivity of the photodetector. The diffraction grating efficiency was not incorporated into the simulations. Fig. 3 shows the relative dye emission (36), the relative responsivity of the photodetector, and the relative power.

In the simulation, the light rays were collimated using the first aspheric lens from the collimation package (350230-A; Thorlabs). The rays were transmitted through the dichroic filter with an index of refraction of 1.458. The long-pass filter was not simulated because the filter did not change the light pathway. The rays were then reflected off a diffraction grating. Finally, the light rays were focused through an additional aspheric lens (350330-A; Thorlabs) onto a square 2.54-mm image plane, which matched the size of the split photodetector. The power and location of the simulated light rays were quantified on the image plane. The light pathway was simulated using an input power of 1.5 nW. The light was detected on the image plane in four equally sized pixels. The sum of the power on two adjacent pixels was the total power from each side of the spectrum. The total power from the higher wavelengths was divided by the power from the lower wavelengths. The ratio of power was measured before and after the spectral shift. The simulated shift was based on a 0.8% decrease in total fluorescence, which corresponded to a shift in the emitted wavelengths of 1 nm. The percentage change in the power before and after the shift was used to estimate the amplitude of the light intensity changes that would be caused by an AP. The results of the simulation determined the selection and placement of the optical components for the design.

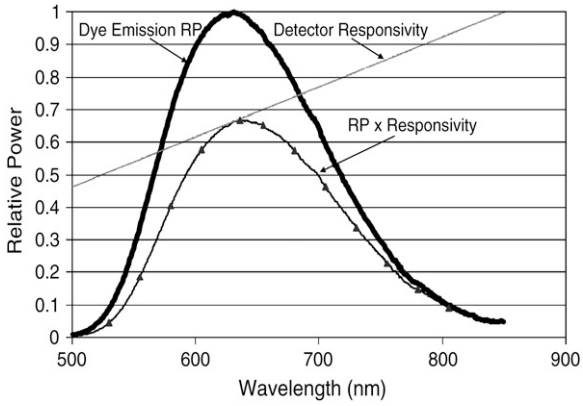

FIGURE 3 The relative power of di-8-ANEPPS dye (*bold line*), photodiode responsivity (*plane line*), and relative power multiplied by the photodiode responsivity with ZEMAX sample wavelengths (*plane line* with *triangles*). The spectra represented are not identical to di-4-ANEPPS, but differences are not expected to be significant.

System alignment

After the channel was built, a helium neon (HeNe) laser (05-LLR-811; Melles Griot, Carlsbad, CA) was used to test the alignment of the optics in the detection pathway. The laser was directed into the tissue fiber through a 632-nm band-pass filter (G42-081; Edmund Optics, Barrington, NJ) and two neutral density filters (ND 30A and ND 13A; Edmund Optics). The photodetector was centered such that each photodiode cell had an equal output voltage. The photodetector was moved with a micromanipulator (H LH; Line Tool, Allentown, PA) in the x and y directions (Fig. 1 shows the coordinate system). The photodetector was also moved in the z and x directions while maintaining equal output voltage after amplification. The slope of the z versus x displacements was the inverse tangent of the alignment angle. The optimal alignment angle was approximately zero when the light was centered and collimated.

Bandwidth calculations and measurement

The electrical bandwidth was also determined for the detector and amplifier circuit, both theoretically and experimentally. The 3-dB cutoff frequency, B, was determined theoretically by

$$B = 1/(2\pi R_f C_f), \quad (4)$$

where R_f is the feedback resistance and C_f is the variable feedback capacitance (37). The junction capacitance from the photodetector was not included in the bandwidth calculation because the unity gain crossover frequency of the operational amplifier was much larger than the bandwidth (37).

Experimentally, the bandwidth was measured using an intensity-modulated red LED (IF-E96; Industrial Fiber Optics, Tempe, AZ). The LED was powered using a waveform generator (33220A; Agilent, Palo Alto, CA), with a sine wave output that had an offset of 1 V and amplitude of 190 mV. The LED was positioned directly in front of the split photodetector to bring the signal produced by the detector circuit to an output peak-to-peak voltage (V_{PP}) of 3 V. The V_{PP} was measured at frequencies ranging 1–50 kHz for several settings of the variable capacitor. The final bandwidth of the circuit was adjusted to 150 Hz (38) using the variable feedback capacitor. The minimal bandwidth was used to maximize the signal/noise ratio (SNR) (39).

Noise calculations

The SNR is typically low in optical signals. Thus, the theoretical noise was also calculated to identify and minimize the dominant noise sources. The noise was a combination of the amplifier noise, the shot noise, and the Johnson noise. The shot noise (i_I) was principally caused by the photodiode current (I). The mean-squared value of the shot noise was determined by

$$i_I^2 = 2e(I + I_d)B, \quad (5)$$

where e is the electron charge (1.602×10^{-19} C), B is the bandwidth, and I_d is the dark current. The dark current is composed of insulation-dispersion current, electrode current, and photocathode current caused by thermal emissions (the dominant contribution) (39). The photodiode dark current was only 5 pA. The photodiode current was estimated from the output signal voltage using Eqs. 1 and 2. For example, a photodiode current of 570 pA produced an output voltage of 627 mV.

The Johnson noise (i_R) is due to the combination of the photodetector resistance and the feedback resistance of 100 MΩ (39). The photodetector resistance includes both series and shunt resistances, which were ignored because of their magnitude (37). The quadratic mean-squared value of the Johnson noise was determined by

$$i_R^2 = 4kTB/R_f, \quad (6)$$

where k is Boltzmann's constant (1.381×10^{-23} J/°K) and T is the temperature (300 K).

The amplification noise current was calculated based on the low bias current of 75 fA (33). The noise associated with the second stage was also found using amplifier noise analysis techniques (40). The total theoretical noise voltage was compared to the experimental noise voltage. The experimental noise voltage ($\text{Noise}_{\text{RMS}}$) was determined by measuring the standard deviation of the detector output during a 20-ms interval before each AP (1).

Rabbit studies

These animal studies were performed under the guidelines of the Duke University Institutional Animal Care and Use Committee. Male Adult New Zealand White rabbits ($n = 5$) were anesthetized with intramuscularly injected ketamine (35 mg/kg) combined with xylazine (5 mg/kg). Heparin (100 mg/kg) and thiopental (20 mg/kg) were given intravenously. Both corneal eye and paw pinch reflexes were used as indicators of adequate sedation. The heart was rapidly excised via median sternotomy and submerged in cold, high potassium Tyrode's solution (24 mM KCl, 123 mM NaCl, 11 mM dextrose, 20 mM $NaHCO_3$, 1.0 mM $NaH_2PO_4 \cdot H_2O$, 1.1 mM $MgCl_2 \cdot H_2O$, and 1.8 mM $CaCl_2$) oxygenated with $95\%O_2/5\%CO_2$. The aorta was cannulated and Langendorff perfused. The heart was placed in a warm bath with normal Tyrode's solution (4.5 mM KCl) and perfused for 1 h to allow the heart to stabilize. Both the flow pressure and temperature were continuously monitored to maintain the physiological range of 60–80 mmHg and 35°C–38°C, respectively. Two electrodes connected to a differential amplifier (Iso-DAM8A; WPI, Sarasota, FL) were used to monitor the electrogram. A force transducer (FORT10; WPI) connected to a bridge amplifier (Bridge 8; WPI) was used to monitor the contraction-induced motion. Transmembrane voltage was measured using standard pulled glass microelectrodes filled with 3 mol/L KCL. The microelectrode signals were low-pass filtered at 500 Hz (Iso-DAM8A; WPI). The tissue was stained with 50 μM di-4-ANEPPS dissolved in ethanol added to the perfusate. Continuous recordings were taken from the base of the heart without BDM.

The atria were removed and the atrioventricular node ablated to prevent spontaneous activations. Baseline endocardial pacing was applied to the right ventricle via a unipolar electrode at a cycle length of 500 ms based on previous investigators (28). The longer cycle length helps to reduce the tissue hypoxia associated with the nonblood Tyrode's perfusion. A shorter cycle length can accelerate the hypoxia due to the higher metabolic demand (41). Control of stimulation and data collection were achieved with LabVIEW 7.0 software, a data collection card (AT-MIO-16E-2; National Instruments (Austin, TX) E-series PCI Card), and a voltage-to-period converter. The signals from the two optical detectors, the microelectrode, the force transducer, and the bath ECG were digitally oversampled at 2 kHz using a 16-bit analog-to-digital converter within a PC.

The signal from shorter wavelengths was divided by the signal from longer wavelengths (25). The signals were normalized by subtracting the minimum value, then dividing the result by the maximum value minus the minimum value. A 20-point median filter was applied to the ratiometric signal to improve the SNR (42). The SNR was determined by

$$\text{SNR} = \text{APA}/\text{Noise}_{\text{RMS}}, \tag{7}$$

where APA is the action potential amplitude and $\text{Noise}_{\text{RMS}}$ is the standard deviation of the signal over the 20-ms interval before each AP (1). The amplitude was the voltage at the AP peak minus the baseline voltage from the median filtered signal. The baseline voltage was the average voltage during the 20 ms preceding the upstroke. The experimental MA was also quantified by measuring the motion ratio. The motion ratio was the APA divided by the peak-to-peak voltage change occurring during each AP (25).

In addition, APD_{70} was measured for both the microelectrode and the optical signals in a single rabbit. The APD was calculated by measuring the interval between the AP upstroke where the voltage rose above 70% of peak amplitude and the repolarization time where the voltage fell below the 70% of the peak amplitude of the AP (1). Recordings were made in the same region (base of the heart) to minimize spatial differences in APD (43). The APD measured for the two conditions were compared using a two-tailed t-test. A p-value < 0.05 was considered significant.

RESULTS

Constructed optical channel

Fig. 4 *A* shows the optical fiber butt-coupled to the LED. The LED was mounted on a heat sink with a fan for cooling. The fiber was secured with epoxy on an aluminum stage. Fig. 4 *B* shows the constructed optical system. The aspheric lens was glued to the outer can of the photodetector. The photodetector was attached to the amplifier, which was mounted to a micromanipulator.

Ray tracing simulations

Fig. 5 shows the simulated path of 636-nm light through the emission pathway. First, the emission light exited the tissue fiber as a round circle with a diameter equal to the fiber core size (125 μm). The light traveled 3.1 mm, which is the focal length of the aspheric lens. This lens collimated the light, which then traveled 26 mm to the dichroic mirror. The mirror was set at a 45° angle, which caused the path of the light to shift by 316 μm. The light traveled 65 mm and reflected off the diffraction grating. The results of the simulation show that the angle of reflection was 49.8° relative to the normal angle of incidence for light at a wavelength of 636 nm. The light traveled a distance of 5 mm to the lens and was focused onto the image plane, which was 1.6 mm away from the lens. The simulated optical design took into account spatial

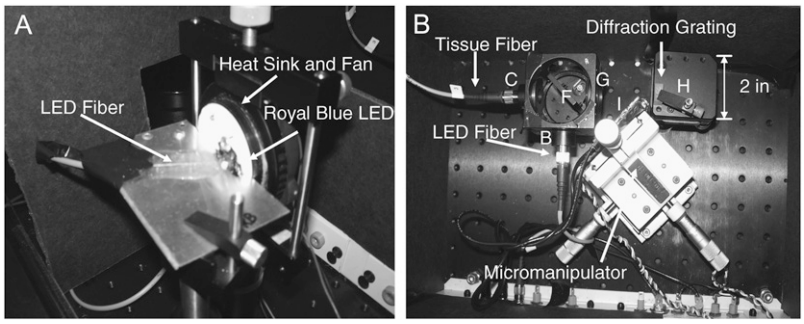

FIGURE 4 (*A*) The fiber is butt-coupled to the royal blue LED. The LED is mounted on a heat sink and fan. (*B*) The constructed optical system. The lens is glued to the outer can of the photodiode, which is mounted to a micromanipulator. The letter labels refer to the block diagram in Fig. 1.

FIGURE 5 ZEMAX simulation at peak wavelength of 636 nm. Our design took into account spatial limitations due to the mounting of the optical parts. The letter labels refer to the optical block diagram in Fig. 1.

limitations needed to mount the optical parts. The results were used to construct the optical channel.

The optimal blaze wavelength for the emission range of 530–805 nm of the Edmund Optics diffraction gratings was 750 nm (vs. 500 nm or 1000 nm). A grating with a blaze wavelength of 750 nm is manufactured with a pitch of either 600 or 1200 grooves/mm. Based on Eq. 3, a 1200 grooves/mm grating can diffract light from 530 nm and 805 nm at an angle of $-39.5°$ and $-75.0°$, respectively. A 600-grooves/mm grating can diffract light from 530 nm and 805 nm at $-18.5°$ and $-28.9°$. The 1200 grooves/mm grating was selected for its larger angular dispersion. The larger angular dispersion created the optimal dispersion onto the split photodetector at a selected distance.

The simulations also allowed us to optimize the distance between the diffraction grating and focusing aspheric lens by simulating the dispersion from the grating over the range of wavelengths encompassed by the dye emission. Fig. 6 *A* shows the ZEMAX simulation using the 12 sampled wavelengths and 1200 grooves/mm grating in the *xz* plane. The central wavelength was 655 nm for equal power distribution on the cells of the split photodetector. Fig. 6 *C* shows each wavelength focused into a circle at a distinct location in the *xy* plane. Fig. 6 *C* also shows an overlay of each detector (1.27×2.54 mm) with the detector gap of 0.127 mm. The top detector collected light from the ''green'' or lower wavelength side of the dye spectrum. The bottom detector collected light from the ''red'' or higher wavelength side of the dye spectrum. Thus, we found that a distance of 5 mm between the diffraction grating and focusing aspheric lens was optimal.

Simulated light rays of 1.5 nW power were coupled into the collection fiber. The ratio of the simulated power on each detector was 1.0093 resulting from 713.1 pW (green detector) and 719.7 pW (red detector). The ratio during an AP changed to 1.0002 resulting from 716.8 pW (green detector) and 716.6 pW (red detector). The percentage change in the green detector, red detector, and ratio were 0.5%, 0.4%, and 0.9%, respectively. The percentage change resulted in the theoretical amplitude from an AP on the green and red detector of ~ 3.7 pW and -3.1 pW, respectively. This converts in the photodetector to a current of 1.50 pA and -1.49 pA (photodetector responsivity at 605 nm = 0.405 A/W, photodetector responsivity at 680 nm = 0.48). The amplification circuit converted the signal to a voltage according to Eq. 1 and amplified the signal according to Eq. 2, resulting in a theoretical voltage arising from the AP of ~ -1.65 mV and 1.64 mV.

Laser measurements

Laser light was used to align the detector with respect to the diffraction grating. The narrow spectral wavelength bandwidth of the laser light produces a spot at a single location on the detector. The voltage from each detector was first measured while moving the micromanipulator left to right along the *x* direction. This measurement was repeated three times at a relative placement of 0 mm, 2.54 mm, and 5.08 mm along the *z* axis. At all three placements, the separation of the peak output voltages from the green and red detectors was 1.905 mm. The separation in the peaks for movement in the *x* direction was due to the element gap in the detector and misalignment of the aspheric lens.

Fig. 7 shows the voltage change as a function of the *y* displacement. The red and green detectors peaked at -650 mV and -645 mV, respectively. The peaks were separated by 0.635 mm. The separation in the peaks from movement in the *y* direction was due to the misalignment of the aspheric lens with respect to the photodetector. Fig. 8 shows measurements taken by moving the photodetector in the *z* and *x* directions to find the angular alignment. The angular alignment is approximately the inverse tangent of the slope. The slope was 0.0008 mm/mm, which corresponds to the detector being $\sim 0.05°$ off axis. This angle could be reduced with a more precise micromanipulator. Fine adjustments (<0.635 μm) were also made in the *x* location of the detector during the experiments to minimize the MA in the ratiometric signal.

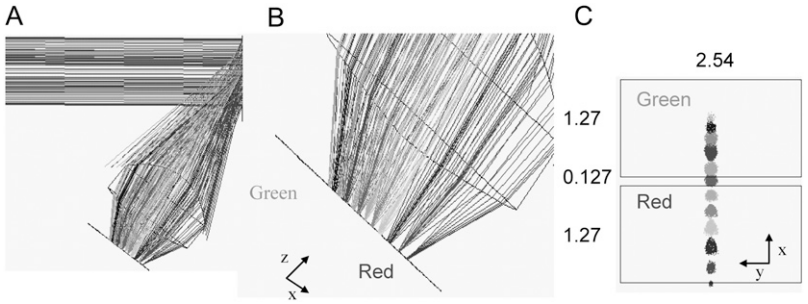

FIGURE 6 (*A*) ZEMAX simulation using 12 sample wavelengths. The central wavelength is 655 nm. (*B*) Zoom in of the *yz* image plane. (*C*) Image on the *xy* image plane with grid representing the photodiode surface. Units are in millimeters.

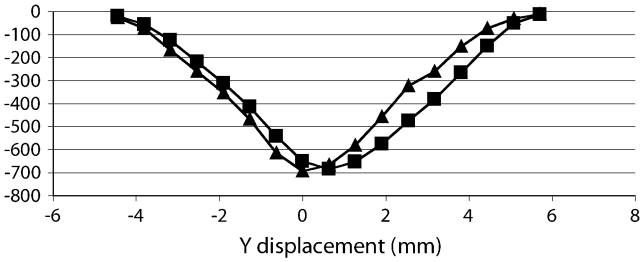

FIGURE 7 *y* displacement voltage changes on each detector. The green detector (*squares*) peaks 0.635 mm from the red detector (*triangles*). The red and green detectors peaked at −650 mV and −645 mV, respectively. This figure shows that the magnitude of the voltage decreases as the laser beam and aspheric lens used to focus the light onto the detector become misaligned.

Bandwidth calculations

The variable capacitor in the feedback of the transimpedance amplifier ranges 0.4–10 pF. This capacitor allows for the variation of the bandwidth based on Eq. 4. The variable capacitor and a resistor of 100 MΩ caused the bandwidth cutoff to range from 160 Hz to 4 kHz. A red LED with varying intensity was used to measure the circuit bandwidth at various capacitor settings. Fig. 9 shows a plot of the voltage amplitude versus the frequency. The 3-dB roll-off frequency was found empirically to range from 110 Hz to 1.5 kHz. The difference between the theoretical and experiment bandwidth was likely due to parasitic capacitance from the traces on the amplifier board. Both detectors were set to have a −3 dB frequency of 150 Hz.

Noise calculations

A low noise split photodiode was selected as the channel detector. The detector was chosen based on its area, responsivity, and shunt resistance. The shunt resistance was 1 GΩ, which was greater than the feedback resistance of 100 MΩ. This difference decreased amplification of noise, voltage offset, and drift (39). The small area (1.27 mm × 2.54 mm) of each cell of the photodiode reduced the junction capacitance, which helped to maximize the bandwidth. The

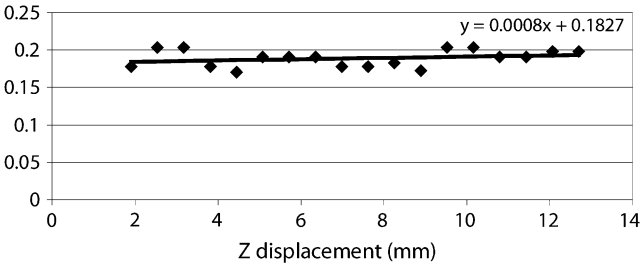

FIGURE 8 *x* displacement as a function of *z* displacement (*squares*). The slope of the linear fit line is 0.0008. The inverse tangent of the slope results in the system at ~0.05° off axis.

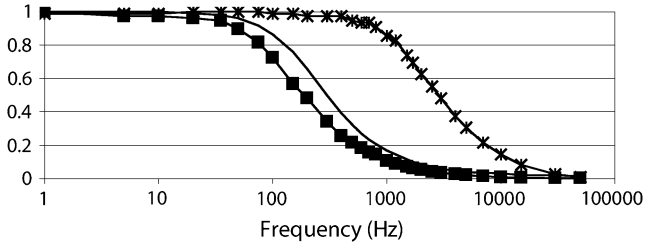

FIGURE 9 Bandwidth range of the amplification circuit. The maximum bandwidth was 4 kHz (*asterisk*). The minimum bandwidth was 110 Hz (*squares*). Both detectors were set to a cutoff bandwidth of 150 Hz (*solid line*).

photodiode also had an interelement gap of only 127 μm. A small gap decreased the signal loss from the center of the emitted spectrum. The responsivity of the photodiode was optimal for the dye's spectrum. The responsivity at 530 nm was 0.27 A/W and 0.6 A/W at 805 nm. The difference in responsivity caused a signal size inequality, which was incorporated into the ZEMAX model and final design.

The largest theoretical noise source was the shot noise from the detector with a mean-square value of 2.8×10^{-26} A^2. The mean-square noise currents from the amplifier and the Johnson noise were 3.6×10^{-30} A^2 and 2.5×10^{-26} A^2, respectively. The total theoretical value of mean-square current noise was 5.2×10^{-26} A^2 (21). This noise was amplified through the first stage and second stage. There was additional amplifier noise Johnson voltage noise from the second stage of 3.0 μV and 52.3 μV (40), respectively. This resulted in a total theoretical of ~257 μV.

Experimentally, the $\text{Noise}_{\text{RMS}}$ was 742 μV on the red detector and 724 μV on the green detector. Frequency analysis showed a peaking at 180 Hz, which was likely due to contributions from 60 Hz sources. The noise spectrum also showed significant contributions above 150 Hz, indicating noise from other sources, possibly the computer and data acquisition card. Both theoretical noise and experimental noise were smaller than the ZEMAX estimated signal size of ~±1.65 mV.

In vitro recordings

Recordings were taken from the rabbit ventricle using the ratiometric channel. Fig. 10 shows the original red and green signals, the raw and filtered ratiometric signals, the force transducer signal, and the signals from the microelectrode. The microelectrode recordings exhibit some artifact during the repolarization phase of the AP. This is due to the tissue-contraction motion, which caused the microelectrodes to partially pull out of the cell membrane. The AP upstroke from the red and green detector was ~± 3 mV. The offset voltages were 341 mV and 132 mV on the green and red portions of the photodiode, respectively. The green offset was higher because reflected and stray illumination light contributed

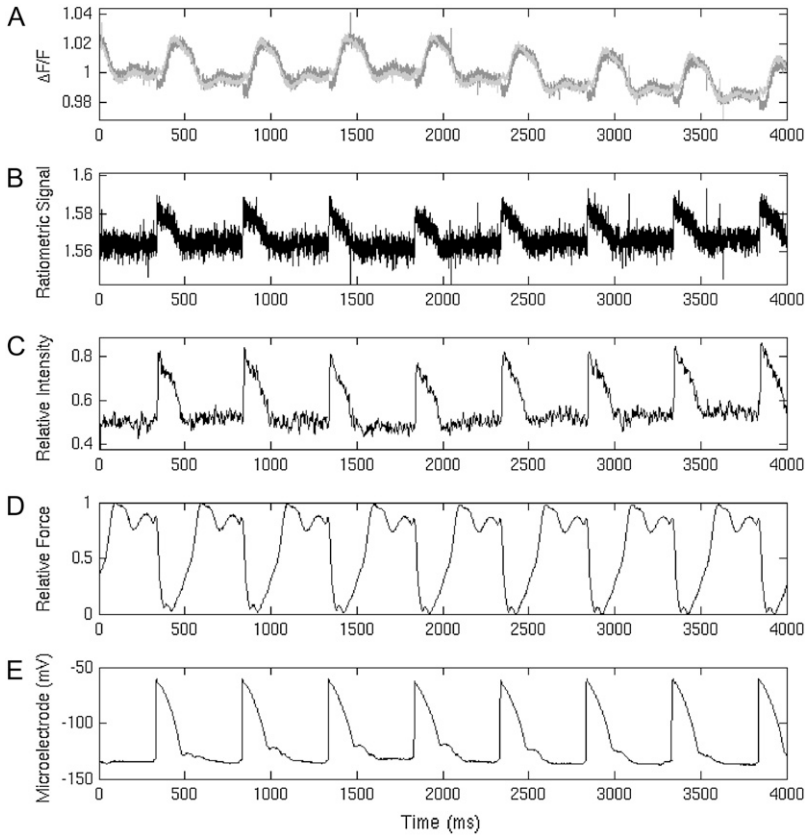

FIGURE 10 Microelectrode and optical rabbit AP recordings. (*A*) Two raw recordings where the AP was not visible due to the MA. The red signal voltage (*black line*) decreases with depolarization, whereas the green signal voltage (*gray line*) increases with depolarization. (*B*) The ratio of the two raw signals. (*C*) The ratio of the two raw signals after median filtering and normalization. The signals were normalized by subtracting the minimum value then dividing the result by the maximum value minus the minimum value. (*D*) The force transducer shows the magnitudes of motion that coincide with the MA in the original signals. (*E*) The microelectrode recordings shown exhibit some artifact during the repolarization phase of the AP. This is due to the tissue-contraction motion causing the microelectrodes to pull out of the cell membrane.

more to this half of the spectrum. The mean total power minus the offset for the results shown was 557.3 pW and 483.2 pW for the red and green detectors, respectively.

The simultaneous microelectrode and optical channel recordings produced an APD_{70} of 137.6 ± 3.3 ms (No. of APs = 7) and 134 ± 8.4 ms (No. of APs = 7), respectively. The difference was found to not be significant (p-value = 0.3). Fig. 10 shows that the original data had MA, which was dramatically reduced after the ratio was calculated.

Table 1 shows the average SNR and motion ratio for all rabbits. The number of continuous APs analyzed from each animal ranged 7–18. For rabbit 5, the average SNR from the optical recordings shown in Fig. 10 was 14.0 ± 2.5 (range 11.1–18.9, No. of APs = 7). The MA was most substantial 80 ms after the AP upstroke. It continued throughout the repolarization and during the diastolic interval. The average motion ratio before ratiometry for the red and green signals was 0.215 ± 0.01 (range 0.20–0.22, No. of APs = 7) and 0.132 ± 0.01 (range 0.116–0.15, No. of APs = 7), respectively. The average motion ratio after ratiometry was 0.69 ± 0.02 (range 0.67–0.71, No. of APs = 7). The difference was statistically significant (p-value = 0.0001).

DISCUSSION

A novel fiber-based ratiometric channel for transmural AP recordings was successfully simulated, constructed, and tested. The system included a royal blue LED to excite the voltage-sensitive dye, a diffraction grating to separate the dye emission spectrum, and a split photodiode to detect the signals from the two bands of the spectrum. The diffraction grating, LED, and split detector replaced the spectrograph, laser, and detector array used in earlier designs (25). These changes decreased the total cost and size, which will allow this channel to be economically expanded into a multichannel system.

TABLE 1 Signal/noise ratio and motion ratio from rabbit studies (value ± SD)

Rabbit	No. of AP's	SNR raw signal	SNR median filter	Red motion ratio	Green motion ratio	Motion ratio
1	18	11.6 ± 1.5	21.9 ± 8.8	0.23 ± 0.03	0.23 ± 0.03	0.66 ± 0.02
2	17	15.95 ± 6.6	30.7 ± 12.5	0.27 ± 0.03	0.30 ± 0.03	0.59 ± 0.19
3	18	11.6 ± 2.1	28.2 ± 15.8	0.20 ± 0.01	0.18 ± 0.01	0.67 ± 0.02
4	17	20.7 ± 3.96	31.5 ± 8.4	0.38 ± 0.03	0.31 ± 0.02	0.69 ± 0.03
5	7	8.8 ± 0.9	14.0 ± 2.5	0.22 ± 0.01	0.13 ± 0.01	0.69 ± 0.02

The ray-tracing simulations were useful for selecting the optical components and layout. The 1200 grooves/mm grating was used because the angular resolution was three times greater than the 600-grooves/mm grating. The larger angular resolution caused a more dramatic spatial dispersion of the emission light. The AP amplitude recorded in the tissue was almost double the AP amplitude predicted by ZEMAX, which assumed detection of 1.5 nW of light with only a 0.8% change in fluorescence. The small percentage change was used to determine if the system could detect a 1-nm shift in the spectrum above the theoretical noise. The experimentally measured signal had less total light detection but a larger percentage change in fluorescence. This fractional change can range 0.0%–8.0% depending on the detection wavelengths (25), experimental setup, and illumination source.

The laser alignment of the detector ensured that the optical components were optimally placed. If the laser spot showed misalignment by greater than the size of the lens (6.33 mm), the lens was not able to focus the light onto the photodiode. This resulted in a decrease in the voltage in both x and y displacement measurements. The angular misalignment was minimal, which helped to ensure the correct wavelengths fell on each half of the photodiode.

Each circuit had a measured 3-dB cutoff bandwidth of 150 Hz. This bandwidth was chosen to ensure that the signal contained the total energy of the AP without including higher frequency noise; ~90% of the total energy of the AP is below 150 Hz (38). The theoretical range of the bandwidth set by the transimpedance amplifier feedback capacitor exceeded the experimental range measured using the intensity varying light source. This difference is likely due to parasitic capacitance from the traces on the amplifier board. The theoretical noise was lower than the experimental noise, which can be additionally reduced with low-pass filtering in the second stage of the amplification circuit.

This system produced a relatively high SNR. These results were likely from illuminating the dye with a royal blue LED. Royal blue light has increased the dye absorption because it emitted at a wavelength that was close to the dye peak absorption. A change in membrane voltage causes a shift in both the absorption and emission spectrum. By exciting the dye at the absorption peak, the intensity changes in the detected signals were primarily due to the shift of the emission spectrum. Royal blue light was also easier to filter from the dye emissions, which is particularly important in ratiometric experiments (25). Filtering out the excitation light reduced the voltage offset at the detectors to ensure an adequate dynamic range in the detector circuit. Royal blue LEDs have been shown to be low noise sources (34) that are also more cost effective than lasers.

Previous work using a fiber-based system with a laser showed an SNR of 16 V/V (3). This was only slightly higher than the recorded average unfiltered SNR of 14 V/V. The SNR could be improved by increasing the excitation light intensity, which will lead to a larger signal. The drawback of increasing the excitation light intensity is photobleaching. Photobleaching will decrease the signal size over time (25).

The motion ratio was an average of 65% lower in the ratiometric signals than the raw signals. It was difficult to measure the motion ratio in the presence of substantial noise. The motion ratio is the upstroke voltage divided by the peak-to-peak voltage during the AP (25). The motion ratio of a signal with no MA will not be close to one if the signal is noisy. This is because random noise increases the peak-to-peak range of voltages during the AP. A raw optical signal (acquired with 10 mM BDM) with almost no visible MA has a filtered SNR of 30.9 V/V but a motion ratio of 0.44 V/V. The motion ratio is useful for quantifying the change in the MA amplitude, but the motion ratio must be considered in the context of the SNR. Knisley et al. reported a better average motion ratio, but the signals also had substantially better SNR (25). The calculated motion ratio for the raw red and green signals was approximately equal to the Knisley et al. results, whereas their ratiometric motion ratio was smaller due to the greater SNR (25).

The channel demonstrated that MA could be almost entirely eliminated using ratiometry. The primary reason the system was successful in reducing MA was matching the two detection pathways. The two bands of emission light were transmitted through the same optical components and then captured by matching photodiodes. This allowed for common detection and amplification of the emission light. The optical signals were simply divided without normalization or background offset subtraction. These novel features allowed this channel to remove MA without the use of BDM.

Limitations

Optical recordings are a spatial average of AP upstrokes from multiple cells. Even at normal conduction velocities, the cells do not activate simultaneously, which increases the upstroke duration of the AP. An optical fiber with a diameter of 125 μm did not have the spatial resolution to overcome this limitation in cell culture studies (44). Previous investigators measured the upstroke duration using 100 μm and 200 μm fibers and concluded that spatial resolution was not a limitation of their system (1,3). The APD measurements found in this study were essentially equal to the microelectrode APD measurements. This finding confirms that the bandwidth, noise, and spatial resolution were not limitations in the novel system.

The channel is a ''proof-of-concept'' design. The channel size must be further minimized for a multichannel system. In a multichannel system, the three-stage micromanipulator can be replaced by a single stage that can be moved in the x direction. Cheaper aluminum parts can also be used to replace the mountings and optical board. The diffraction grating is a simple and cost effective device that can easily be incorporated into a multichannel mapping system. For example, a grating can be used to replace the dichroic mirror for

separating the emission spectrum of the dye in the previously described low cost optical system (45). Though the diffraction grating does not have the same efficiency as the dichroic mirror, it was shown to be an effective addition to the channel.

CONCLUSIONS

This channel dramatically reduced MA, allowing AP recordings without BDM that would otherwise not be possible. Real time AP recordings can now be taken under various pacing protocols without signal averaging. The channel has a high SNR that ranged from 14 V/V to 32 V/V, which was comparable to previously designed systems. The channel was also able to record APs that were comparable to microelectrode recordings with no statistically significant difference in the APD. In summary, a fiber-based ratiometric system was able to capture the AP during heart motion without the use of a mechanical-uncoupling drug.

We gratefully acknowledge discussions of this work with Wanda Krassowska, Joseph Izatt, Salim Idriss, Ned Rouse, and Ellen Dixon-Tulloch.

We gratefully acknowledge the financial support of the National Institutes of Health under grant 1R01-HL-72831. N.H.B. acknowledges the financial support of the National Institutes of Health under grant HL072831-02S1 and F31 Eb003389-01A1. H.M.D. and D.J.G. acknowledge the financial support of the National Science Foundation under grant PHY-0243584.

REFERENCES

1. Byars, J. L., W. M. Smith, R. E. Ideker, and V. G. Fast. 2003. Development of an optrode for intramural multisite optical recordings of Vm in the heart. *J. Cardiovasc. Electrophysiol.* 14:1196–1202.
2. Caldwell, B. J., I. J. LeGrice, D. A. Hooks, D. C.-S. Tai, A. J. Pullan, and B. Smaill. 2005. Intramural measurement of transmembrane potential in the isolated pig heart: validation of a novel technique. *J. Cardiovasc. Electrophysiol.* 16:1001–1010.
3. Hooks, D. A., I. J. LeGrice, J. D. Harvey, and B. H. Smaill. 2001. Intramural multisite recording of transmembrane potential in the heart. *Biophys. J.* 81:2671–2680.
4. Krauthamer, V., H. Bryant, C. Davis, and T. Athey. 1991. Action potential-induced fluorescence changes resolved with an optical fiber carrying excitation light. *J. Fluoresc.* 1:207–213.
5. Neunlist, M., S. Zou, and L. Tung. 1992. Design and use of an optrode for optical recordings of cardiac action potentials. *Eur. J. Physiol.* 420: 611–617.
6. Kodama, I., I. Sakuma, N. Shibata, S. B. Knisley, R. Niwa, and H. Honjo. 2000. Regional differences in arrhythmogenic aftereffects of high intensity DC stimulation in the ventricles. *PACE.* 23:807–817.
7. Wiggins, J. R., J. Reiser, D. F. Fitzpatrick, and J. L. Bergey. 1980. Inotropic actions of diacetyl monoxime in cat ventricular muscle. *J. Pharmacol. Exp. Ther.* 212:217–224.
8. Li, T., N. Sperelakis, R. E. Teneick, and R. J. Solaro. 1985. Effects of diacetyl monoxime on cardiac excitation-contraction coupling. *J. Pharmacol. Exp. Ther.* 232:688–695.
9. Efimov, I. R., and T. N. Mazgalev. 1998. High-resolution three-dimensional fluorescent imaging reveals multilayer conduction pattern in the atrioventricular node. *Circulation.* 98:54–57.
10. Dillon, S. M. 1991. Optical recordings in the rabbit heart show that defibrillation strength shocks prolong the duration of depolarization and the refractory period. *Circ. Res.* 69:842–856.
11. Wu, J. S., M. Biermann, M. Rubart, and D. P. Zipes. 1998. Cytochalasin D as excitation-contraction uncoupler for optically mapping action potentials in wedges of ventricular myocardium. *J. Cardiovasc. Electrophysiol.* 9:1336–1347.
12. Baker, L. C., B. London, B. R. Choi, G. Koren, and G. Salama. 2000. Enhanced dispersion of repolarization and refractoriness in transgenic mouse hearts promotes reentrant ventricular tachycardia. *Circ. Res.* 86: 396–407.
13. Baker, L. C., R. Wolk, B. R. Choi, S. Watkins, P. Plan, A. Shah, and G. Salama. 2004. Effects of mechanical uncouplers, diacetyl monoxime, and cytochalasin-D on the electrophysiology of perfused mouse hearts. *Am. J. Physiol. Heart Circ. Physiol.* 287:H1771–H1779.
14. Bergey, J. L., J. D. McCallum, and K. Nocella. 1981. Antiarrhythmic evaluation of verapamil, nifedipine, perhexiline and skf 525-A in four canine models of cardiac arrhythmias. *Eur. J. Pharmacol.* 70: 331–343.
15. Blanchard, E. M., G. L. Smith, D. G. Allen, and N. R. Alpert. 1990. The effects of 2,3-butanedione monoxime on initial heat, tension, and aequorin light output of ferret papillary muscles. *Pflugers Arch.* 416: 219–221.
16. Gwathmey, J. K., R. J. Hajjar, and R. J. Solaro. 1991. Contractile deactivation and uncoupling of crossbridges: effects of 2,3-butanedione monoxime on mammalian myocardium. *Circ. Res.* 69:1280–1292.
17. Qin, H., M. W. Kay, N. Chattipakorn, D. T. Redden, R. E. Ideker, and J. M. Rogers. 2003. Effects of heart isolation, voltage-sensitive dye, and electromechanical uncoupling agents on ventricular fibrillation. *Am. J. Physiol. Heart Circ. Physiol.* 284:H1818–H1826.
18. Cheng, Y., K. Mowrey, I. R. Efimov, D. R. Vav Wagoner, P. J. Tchou, and T. N. Mazgalev. 1997. Effects of 2,3-butanedione monoxime on atrial-atrioventricular nodal conduction in isolated rabbit heart. *J. Cardiovasc. Electrophysiol.* 8:790–802.
19. Banville, I., and R. Gray. 2002. Effects of action potential duration and conduction velocity restitution and their spatial dispersion on alternans and the stability of arrhythmias. *J. Cardiovasc. Electrophysiol.* 13: 1141–1149.
20. Kettlewell, S., N. L. Walker, S. M. Cobbe, and G. L. Smith. 2003. The electrophysiological and mechanical effects of 2,3-butane-dione monoxime and cytochalasin-D in the Langendorff perfused rabbit heart. *Exp. Physiol.* 89:163–172.
21. Biermann, M., M. Rubart, A. Moreno, J. Wu, A. Josiah-Durant, and D. P. Zipes. 1998. Differential effects of cytochalasin D and 2,3 butanedione monoxime on isometric twitch force and transmembrane action potential in isolated ventricular muscle: implications for optical measurements of cardiac repolarization. *J. Cardiovasc. Electrophysiol.* 9:1348–1357.
22. Lee, M.-H., S.-F. Lin, T. Ohara, C. Omichi, Y. Okuyama, E. Chudin, A. Garfinkel, J. N. Weiss, H. Karagueuzian, and P.-S. Chen. 2001. Effects of diacetyl monoxime and cytochalasin D on ventricular fibrillation in swine right ventricles. *Am. J. Physiol. Heart Circ. Physiol.* 280:H2689–H2696.
23. Jalife, J., G. E. Morley, N. Y. Tallini, and D. Vaidya. 1998. A fungal metabolite that eliminates motion artifact. *J. Cardiovasc. Electrophysiol.* 9:1358–1362.
24. Efimov, I. R., D. T. Huang, J. M. Rendt, and G. Salama. 1994. Optical mapping of repolarization and refractoriness from intact hearts. *Circulation.* 90:1469–1480.
25. Knisley, S. B., R. Justice, W. Kong, and P. Johnson. 2000. Ratiometry of transmembrane voltage-sensitive fluorescent dye emission in hearts. *Am. J. Physiol. Heart Circ. Physiol.* 279:H1421–H1433.
26. Montana, V., D. L. Farkas, and L. M. Loew. 1989. Dual-wavelength ratiometric fluorescence measurements of membrane potential. *Biochemistry.* 28:4536–4539.
27. Fromherz, P., and A. Lambacher. 1991. Spectra of voltage-sensitive fluorescence of styryl-dye in neuron membrane. *Biochim. Biophys. Acta.* 1068:149–156.
28. Tai, D. C.-S., B. J. Caldwell, I. J. LeGrice, D. A. Hooks, A. J. Pullan, and B. H. Smaill. 2004. Correction of motion artifact in transmembrane

voltage-sensitive fluorescent dye emission in hearts. *Am. J. Physiol. Heart Circ. Physiol.* 287:H985–H993.

29. Fluhler, E., V. G. Burnham, and L. M. Loew. 1985. Spectra, membrane binding, and potentiometric responses of new charge shift probes. *Biochemistry.* 24:5749–5755.
30. Loew, L., L. B. Cohen, J. Dix, E. N. Fluhler, V. Montana, G. Salama, and W. Jain-young. 1992. A naphthyl analog of aminostyryl pyridium class of potentiometric membrane dyes shows consistent sensitivity in a variety of tissue, cell and model membrane preparations. *J. Membr. Biol.* 130:1–10.
31. Bullen, A., and P. Saggau. 1999. High-speed, random-access fluorescence microscopy: II. Fast quantitative measurements with voltage-sensitive dyes. *Biophys. J.* 76:2272–2287.
32. Liu, Q., and N. Ramanujam. 2004. Experimental proof of the feasibility of using an angled fiber-optic probe for depth-sensitive fluorescence spectroscopy of turbid media. *Opt. Lett.* 29:2034–2036.
33. Burr-Brown Corporation. 1994. Application Bulletin: Designing Photodiode Amplifier Circuits with OPA128. Burr-Brown Corporation, Tucson, AZ.
34. Entcheva, E., Y. Kostov, E. Tchernev, and L. Tung. 2004. Fluorescence imaging of electrical activity in cardiac cells using an all-solid-state system. *IEEE Trans. Biomed. Eng.* 51:333–341.
35. Jenkins, F. A., and H. E. White. 1976. Fundamentals of Optics, 4th ed. McGraw-Hill, New York.
36. Molecular Probes Inc. 2006. Spectra—Di-8-ANEPPS/Lipid. Eugene, OR.
37. Graeme, J., editor. 1996. Photodiode Amplifiers: Op Amp Solutions. McGraw-Hill, Boston.
38. Girouard, S. D., K. Laurita, and D. Rosenbaum. 1996. Unique properties of cardiac action potentials recorded with voltage sensitive dyes. *J. Cardiovasc. Electrophysiol.* 7:1024–1038.
39. Donati, S. 2000. Photodetectors: Devices, Circuits and Applications. Prentice-Hall, Upper Saddle River, NJ.
40. Texas Instruments Inc. 1998. Noise Analysis in Operational Amplifier Circuits. Texas Instruments Incorporated, Dallas, TX.
41. Pitruzzello, A. M., W. Krassowska, and S. F. Idriss. 2007. Spatial heterogeneity of the restitution portrait in rabbit epicardium. *Am. J. Physiol. Heart Circ. Physiol.* 292:H1568–H1578.
42. Witkowski, F. X., P. A. Penkoske, and L. Leon. 2001. Optimization of temporal filtering for optical transmembrane potential signals. *In* Optical Mapping of Cardiac Excitation and Arrhythmias. D. S. Rosenbaum and J. Jalife, editors. Futura Publishing, Armonk, NY. 79–92.
43. Sicouri, S., and C. Antzelevitch. 1991. A subpopulation of cells with unique electrophysical properties in the deep subepicardium of the canine ventricle. The M cell. *Circ. Res.* 68:1729–1741.
44. Rohr, S., and J. Kucera. 1998. Optical recording system based on a fiber optic image conduit: assessment of microscopic activation patterns in cardiac tissue. *Biophys. J.* 75:1062–1075.
45. Idriss, S. F., and A. M. Pitruzzello. 2006. A low-cost high-efficiency fiber-optic coupler for recording action potentials within the myocardial wall. *IEEE Trans. Biomed. Eng.* 53:1708–1711.